RSC Advances

ROYAL SOCIETY OF CHEMISTRY

www.rsc.org/advances

Room Temperature Lead-Free Relaxor-Antiferroelectric Electroceramics for Energy Storage Applications

Hitesh Borkar[1], V N Singh[1], B P Singh[1], M Tomar[2], Vinay Gupta[3], Ashok Kumar[1,*]

[1]CSIR-National Physical Laboratory, Dr. K. S. Krishnan Marg, New Delhi 110012, India
[2]Department of Physics, Miranda House, University of Delhi, Delhi 110007, India
[3]Department of Physics and Astrophysics, University of Delhi, Delhi 110007, India

Abstract

Round the globe, scientific communities have been searching for new materials for "green" energy, producing efficiently both high power as well as high energy density. Relaxor ferroelectrics (RFEs) have shown immense potential to achieve this goal. We report fabrication of $(Na_{0.42}Bi_{0.44}Al_{0.06}Ba_{0.08})TiO_3$ (NBAT-BT)), a lead-free-relaxor antiferroelectric ceramic, via a conventional solid-state reaction method. A small fraction of trivalent cations (Al^{3+}) doping at Na^{+1}/Bi^{3+} sites develop anti-polar phase in the ferroelectric matrix which in turn changes its functional properties. Rietveld refinement suggests existence of both tetragonal and rhombohedral phases that is well supported by d-spacing values obtained in high resolution transmission electron microscopy (HRTEM) studies. Elemental analysis confirms the stoichiometry of the system and matches the starting composition well within the experimental uncertainty (+/-10%) of secondary electron microscopy (SEM) and HRTEM data. Raman spectra suggest the substitution of Al^{3+} cation at A-site sublattice. Temperature-dependent dielectric spectra show frequency dependent dielectric dispersion near 80-110 °C, high dielectric loss at high probing frequency, and a non-linear Vogel-Fulcher relation, substantiating the relaxor-antiferroelectric (r-AFE) nature of NBAT-BT. A second order diffuse anti/ferro-electric to paraelectric phase transition near 230-240°C was observed which follows a modified Curie-Weiss law. The energy density was calculated from polarization-electric field (P-E) loops and

dielectric-electric field (ε-E) plot. The values were in the range of 0.4-0.6 J/cm^3, which is reasonably good for bulk polar material. NBAT-BT shows much slimmer AFE hysteresis above its relaxor FE phase transition; that favors the enhanced energy storage capacity at elevated temperature in the depolarized paraelectric region.

Corresponding Author: Dr. Ashok Kumar (ashok553@nplindia.org)

Introduction:

Nowadays green energy generation and storage materials and devices are a major thrust area of research and technology. Dielectric capacitors are well-known for their high power density and discharge capability (time constant ~ μs). Among the dielectrics, ferroelectrics usually possess higher dielectric constants and fast discharge time (~ ns) that make them suitable candidates for high energy density storage applications [1,2]. At present, the energy density of dielectrics/ferroelectrics materials is poor compared to supercapacitors and the Li-ion batteries [3]. The low energy density of polar dielectrics is due to low breakdown field, high dielectric saturation, square hysteresis (dielectric loss) and large leakage current under the application of electric field [4,5]. Short range orders (SRO) relaxor embedded in anti-ferroelectric matrix has immense potential in designing new polar dielectrics for high energy storage applications due to their slim polarization-electric field (P-E) hysteresis. Anti-ferroelectrics have linear and non-linear hysteresis (in E) that yield the largest energy storage area in P-E hysteresis in any polar dielectrics [6]. This indicates that an antiferroelectric matrix embedded with polar-nano-regions (PNRs) (relaxor-antiferroelectric) are suitable candidates for moderate power and energy-density applications. Such system may allow us to understand new capacitor materials having high

dielectric constant and energy storage capacity. Lead-based relaxor antiferroelectric PLZT (lead-lanthanum-zirconate-titanate) thick films show high energy density (up to 58.1 J/cm^3 at 2.8 MV/cm). However, the environmental issues and regulations to ban toxic materials by several countries are forcing the development of lead-free (non-toxic) research [7,8].

The direct way to calculate the energy density and energy storage capacity per unit volume of the material are as follows:

$$U = \int EdD = \int EdP \quad \text{.....(1)}$$

where D = $\varepsilon_0 E$+P, since polarization of ferroelectric dielectrics is very high so D ≈ P.

$$\overline{U} = \frac{1}{2}\frac{CV^2}{volume} = \frac{1}{2}\frac{\varepsilon\varepsilon_0 A E_b^{\,2} t_{die}^{\,2}}{t_{die}.A.t_{die}} = \frac{1}{2}\varepsilon\varepsilon_0\eta^2 E_b^{\,2} \qquad [J/cm^3] \quad \text{.....(2)}$$

where C is capacitance; E, applied electric field; P, polarization; V, voltage; ε, dielectric constant of the material, ε_0 dielectric constant of vacuum, and E_b breakdown field. The dielectric is susceptible to breakdown under the application of constant high external field. To avoid any premature breakdown of the capacitor, it is advisable to use external field almost half of the breakdown field, i.e., $V=\eta V_b \sim \eta E_b$ ($0<\eta<1$) [9].

The lead free $(1-x)(Na_{0.50}Bi_{0.50})TiO_3$-$xBaTiO_3$ (NBT-BT) system is well known for its excellent piezoelectric properties, several structural phase transitions, large variation in functional properties due to composition tunability, and coexistence of relaxor-polar and antipolar phases [10,11,12,13,14]. The NBT-BT system illustrates depolarization properties [that is, transition of ferroelectric FE to AFE-like phases] in the temperature range of 100 to 190 °C depending on the composition of BT near the morphotropic phase boundary (MPB) [15,16,17]. The rhombohedral (FE) to high-temperature tetragonal diffuse phase transition (220-320°C) is achieved via an intermediate AFE-like phase transition. Ma et al. showed the presence of nano-

size short-range polar-regions for the compositions ($0.07 \leq x \leq 0.09$) that lead to the relaxor-AFE phase boundary. Recently they also established a new phase boundary in NBT-BT measuring the precise positions of oxygen octahedral tilting in multi-domain perovskite ferroelectrics using electron diffraction analysis [18]. Another aspect, nonstoichiometry, is equally important in determining piezoelectric properties and depolarization temperatures. Many research groups have extensively studied nonstoichiometry-microstructure-property relationship [19,20,21,22,23,24,25]. In general, it has been accepted that Na^{+1} cations deficiencies and excess Bi cations lead to decrease in depolarization temperature and develop the AFE-like micro-polar regions in ferroelectric matrix. The ratio of A-site cations (Na^{+1} and Bi^{+3}) was always considered as unity; however, in reality it is very hard to maintain such ratio, due to the volatile nature of both Na- and Bi-cations. Guo et al. have carried out extensive study on compositional modulation of NBT-BT system and showed that AFE-like phase can be induced at ambient temperature [26].

Lead-based relaxor/anti-ferroelectrics have been thoroughly investigated for high energy density applications and have shown high energy storage capacity [27]. Polymer relaxor ferroelectric thin films show high energy density (10-25 J/cm^3) with very fast discharge capacity [3]. Ceramic-polymer and ceramic-glass composite systems are also potential candidates for high energy density capacitors due to their high breakdown strength and low dielectric saturation [28,29,30]. Polar or non-polar multilayers and superlattices thin films have been investigated almost material science techniques and it has also shown tremendous potential in energy applications with proper design of polar-nonpolar layers [3].

In this paper, we report the effect of Al^{3+} cations (valance state (+3) of A-site) substitution on the relaxor-AFE properties of NBAT-BT. A minimum Al^{3+} cations percentage is

incorporated in the system to avoid any pyrochlore or impurity phase. The microstructure-property relationship is discussed in the context of its ability to store energy.

Experimental:

Polycrystalline ceramic samples of $(Na_{0.42}Bi_{0.44}Al_{0.06}Ba_{0.08})TiO_3$ (initial precursor compositions $(Na_{0.43}Bi_{0.43}Al_{0.06})TiO_3$-$Ba_{0.08}TiO_3$)) were prepared by conventional solid state reaction techniques. The high purity (~ 99.9%) initial precursors Na_2CO_3, $BaCO_3$, Bi_2O_3, TiO_2 and Al_2O_3 (Sigma Aldrich) were mixed at ambient conditions and then homogenous blend with IPA (Isopropyl alcohol), using agate mortar-pestle by grinding for 2 hours. The mixed precursors were first calcined at an optimized temperature 1000 ^oC for about 4 h in a high purity alumina crucible. Calcined powder was reground and then mixed with a binder (Polyvinyl alcohol) in order to prepare the circular disc-shape pellets. The average diameter and thickness of the pellets were 13 mm and 1~1.5 mm, prepared under uniaxial pressure of 5-6 ton per square inch. The prepared pellets were subsequently sintered at an optimized temperature 1200^oC for 8 hours to achieve the 92-95 % of theoretical density. Room temperature X-ray diffraction pattern was taken using CuK_α radiation (λ= 1.5460 Å, Bruker D8 Advance) over a wide range of Braggs angle ($20^o<\theta< 80^o$) to identify the structure and phase purity of sintered ceramic pellets.

Grain growth, surface morphology, and elemental analysis on sintered pellets were carried out using scanning electron microscope (SEM, Zeiss EVO MA-10). Crystal structure, atom positions in lattice planes, grain orientations, and size were determined by using Technai G20-stwin, 300 kV, High Resolution Transmission Electron Microscope (HRTEM). To measure the electrical properties, metal-insulator-metal capacitor structures were prepared using the silver paint coating on both sides of the ceramic pellets. Temperature-dependent dielectric measurements were carried out on metalized pellets at various frequencies (1 KHz~1MHz) and temperature range using an LCR meter (4200-SCS Analyzer) at an oscillating amplitude of 0.5

V. Ferroelectric P-E hysteresis loops and leakage current were measured by using a Radiant Ferroelectric Tester. Room temperature Raman studies were carried out using Renishaw inVia Reflex Raman spectrometer, UK (with an excitation source of 514.5 nm) with a resolution less than 1.0 cm^{-1}.

Results and Discussion:

A. Crystal Structure:

Rietveld refinement on the unpoled x-ray diffraction data were tested for the determination of amount of both the tetragonal (space group *P4mm*) and rhombohedral (space group *R3c*) crystal structure as reported earlier for the MPB of the NBT-BT system [31]. (Na, Bi, Al, Ba) and Ti ions were added to A and B sites of ABO_3 perovskite respectively using the occupancy constrain relation $n_{A^{2+}} = 1 - n_{B^{4+}}$. The observed diffraction peaks were simulated with a Psuedo-voigt profile function. The normal procedures for the Rietveld refinement have been followed for the simulation of experimental x-ray data. Anisotropic values of atomic (thermal) displacement (Debye-Waller factor) parameters are obtained in the stable and best fit [32]. The reliability factors for rhombohedral crystal structure are R_p = 9.43 %, R_{wp} = 12.1 %, χ^2 = 2.89, R_{exp} = 6.98 %, R_{Bragg} = 5.46% and lattice constants (a = 5.5173 Å, b= 5.5173 Å, c= 13.4722 Å) and for tetragonal are R_p = 7.61 %, R_{wp} = 10.4 %, χ^2 = 2.09, R_{exp} = 6.97 %, R_{Bragg} = 3.94%, and lattice constants (a = 3.8964 Å, b= 3.8964 Å, c= 3.9255 Å). The reliability factors are in good agreement with those reported by Wook *et al*. [31]. Fig. 1 (a) & (b) show a very good agreement between the experimental and simulated profile data for the above mentioned reliability factor values. All the prominent Bragg peaks were successfully indexed for both the crystal structures. The incorporation of a very small fraction of Al^{3+} cations hardly affects the lattice parameters,

and it is not easy to detect the elemental compositions and crystallographic positions with low resolution XRD and HRTEM results. Fractional atomic coordinates, positions, occupancies and other fitted parameters are presented in Table 1. The d-spacing of different planes calculated using the HRTEM data matches well with tetragonal/rhombohedral crystal structure. The difference in the d-spacing for both the systems was detectable only after two decimal points of d-spacing data (<1%). It would be unwise to report the exact lattice planes for either system with the given HRTEM image resolution. XRD analysis was carried on unpoled-polycrystalline samples to obtain the ratio of both crystal phases. The results obtained from the refined intensity of the coexisting rhombohedral (r-phase) and tetragonal phases (t-phase) suggests that NBAT-BT is composed of 48(+/- 5) % r-phase and 52 (+/-5) % t-phase. The existence of twin boundaries and their separate phases can also be seen in the HRTEM image of (110) plane with their fast Fourier transformation (FFT) as depicted in figure 3. The intensity of both phases is slightly different with each other over large area of the crystal surface confirms the presence of both phases and its distribution throughout the matrix.

B. Morphology, Size and d-spacing of Crystal:

The surface morphology and grain growth can be seen from the SEM image (inset of Fig.1 (a)) of as-grown pellets. They indicate fine square grains with average size of 1-5 μm. These grains are highly packed with little porosity. EDAX analysis for the proper elemental composition was carried out on large areas of the pellets and on individual grains. A reliable matching elemental ratio was obtained between precursor and the final product. The final elemental ratio is given in the Table2. To better understand the microstructure-property relation, electron diffraction patterns were taken on various sintered ceramic grains. These grains were

obtained from mechanically milled powder of the sintered pellets. The ultra-sonicated dispersions of fine particles were put on carbon-coated copper grid for HRTEM study. The TEM results from the representative grains are shown in Fig 2. (a-f). Fig. 2(a) shows the fine nano-grains surrounded by larger grains > 100 nm. To check the real distribution of the fine grains, TEM imaging was carried out on different particles of the NBAT-BT. Each time it showed uneven distribution of nanoparticles in the matrix. Fig. 2(b) elucidates the small ordered regions (different contrast compared to surrounding) in the matrix; may represent the PNRs, responsible for large dielectric dispersion near room temperature. The d-spacing for both the crystal systems were imaged for different parts of the grains in HRTEM studies. Fig.2 (c-f) represents different lattice planes of NBAT-BT crystal that matched well with the d-spacing obtained for the tetragonal crystal structure from the x-ray data (Rietveld analysis). The observed planes for both crystal systems vary only in the third decimal. This is hard to distinguish form the present HRTEM image resolutions. However, one point is clear from all these TEM images: these planes are not single crystalline in nature; they possesses poly-crystalline contrast, chemical in-homogeneities, discontinuity, disordered, and a mixture of long and short range ordering. These observations support the relaxor-AFE character of the samples. Therefore, a relaxor-AFE phase and coexistence of rhombohedral-tetragonal phase at room temperature are proposed near the MPB with substitution of small amount of trivalent cations. Fig. 3(a &b) shows the FFT and inverse FFT (IFFT) images of NBAT-BT poly-crystals. FFT and IFFT analysis were carried out on the large area HRTEM image which shows the co-existence of both the phases with slight different in their crystallographic planes intensities and positions. The presence of both t-phase and r-phase (101) and (110) planes can be seen from the Fig.3 respectively. Atomic contrasts on various atomic planes and small regions with different microstructure intensity (circled on the

TEM image) can be seen in the Fig. 3 (b) suggest the existence of chemical inhomogeneity in the systems support the microstructure-property relations. HRTEM image also revealed that some crystal area having large number of twin boundaries promote the formation of twin phases (as highlighted by the transparent lines).

C. Raman Spectroscopy:

Raman spectroscopy is a versatile tool for detection of subtle structural distortions, local defects, compositional inhomogeneity, and different ordering states in perovskites structure. Raman spectra of the NBAT-BT are analyzed using the damped harmonic oscillator model (DHO). [33] The observed vibrational modes are analyzed and fitted with the spectral response function.

$$S(\nu) = \sum_i \frac{\chi_{0i}\Gamma_i\nu_{0i}^2\nu}{(\nu^2-\nu_{0i}^2)+\Gamma_i^2\nu^2}F(\nu,T) \quad \text{.....(3)}$$

where $F(\nu,T)=[n(\nu)+1]$ (Stokes scattering) and $n(\nu)=[exp(h\nu/\kappa T)-1]^{-1}$. The parameters in Eq. (1) amplitude χ_0 (in arbitrary units), the mode frequency ν_0, the damping constant Γ, and the temperature T, describe each phonon modes as a damped harmonic oscillator. Figure 4 (a-d) shows the Raman spectra and their DHO model fitting over large frequency regions of NBAT-BT ceramics. The intensities of low frequency vibrational modes are six times higher than the high frequency modes that make it difficult to DHO fit for all the Raman modes with single frequency window. Group theory predicts $4A_1$(IR,R)+9E (IR,R) optical modes for rhombohedral *R3c* phase, and 7(IR+R)+1R modes for tetragonal *P4mm* phase.[34] Fig. 4(a) illustrates the Raman spectra of NBAT-BT electro-ceramics which is in accordance with the previous reported data on NBT-BT.[35,36] In general, Raman bands are relatively broad due to chemical inhomogeneity, overlapping of different Raman vibrational modes, and chemical potential of four cations with different atomic mass and radii at A-site sublattice. Fig. 4(b,c) shows three

Raman active modes at 116 cm^{-1}, 153 cm^{-1}, and 183 cm^{-1} below 200 wavenumber. A low frequency 96 cm^{-1} mode was observed, however, it cannot be trustworthy due to experimental limitation of Renishaw inVia Reflex Raman spectrometer. The variation in the intensity of the various peaks below 200 cm^{-1} could be a result of the substitution of Al(3+) at A-site sublattice. The presence of four cations (Al/Na/Bi/Ba) causes difficulty to analyze the mass and radii effects on low frequencies Raman modes. The overlapped Raman spectra of the specimens is mainly due to the random distribution of Na, Al, Bi and Ba cations breaks the k = 0 selection rule and permits phonons from the entire Brillouin zone to become Raman active. Four Raman active modes were observed for the medium frequency range (250-550 cm^{-1}) which represent the oxygen ion vibration with different A and B-site cations and also due to dielectric leakage [36]. The high frequency Raman modes in the region of 600–900 cm^{-1} have been attributed to B-site sublattice (Ti–O–Ti stretching modes), in which the vibaration around 600-700 cm^{-1} corresponds to edge shared octahedral, 748 cm^{-1} to corner sharing octahedral, and at 805/859 cm^{-1} short Ti–O bonds in the distorted TiO_6 octahedral. These bands matches with the vibration of pure NBT-BT ceramics near the morphotropic phase boundaries (MPB). The bands position of high frequency Raman modes indicate that negligible effect of the Al doping at the B-site. Low frequency bands position and intensity indicates substantial influence of Al cation at A-site sublattice.

D. Dielectric and Tangent loss Spectroscopy:

Figure 5(a) & (b) show the dielectric constant (ε) and tangent loss (tanδ) data as functions of temperature at different frequencies. Two well-defined ε and tanδ anomalies can be seen near 80°C -120 °C and 240 °C, respectively. The first phase transition shows well-defined ε and tanδ dispersion with shifting of dielectric maxima temperatures (T_m) towards higher temperatures

with increase in frequency. The T_m values of the dielectric spectra were fitted with a nonlinear Vogel- Fulcher (VF) relation (Equation 3) as shown in the inset of Figure 5(d) [37,38,39].

$$f = f_0 \exp\left(-E_a / k_B (T_m - T_f)\right) \quad \text{.....(4)}$$

where f is the experimental frequency; f_0, the pre-exponential factor; E_a, the activation energy; k_B, the Boltzmann constant; and T_f, the static freezing temperature. The fitted parameters E_a = 0.42 eV, f_0 = 5.48x10^7 Hz, and T_f = 307 K matches with numerical values for other relaxor systems within the limit of their uncertainties [37]. The second phase transition is a diffused phase transition that fits well with the modified Curie-Weiss laws, as shown in Fig. 5(c) [37]. The value of diffusivity exponent, $\gamma \sim 1.78$ indicates that the system has broad dielectric relaxation and a higher level of disorder. The degree of disorder reveals that dynamic PNRs persist far above the lower phase transition temperature. The tangent loss illustrates a second anomaly below the second phase transition temperature that is normal for diffuse-type FE to PE phase transitions. It follows similar trend of frequency response as that of dielectric constant; however, the degree of tangent loss dispersion is very high (170-200°C) compared to dielectric data near the 2nd phase transition. These observations favor high crystal disorder till the 2nd phase transition. One should note that the dielectric loss data and their dispersion with frequency and temperature provide more reliable information than the dielectric constant values alone. The functional properties, variation in T_m and dielectric loss depends on the probe frequencies that is mainly due to the presence of short range ordering (SROs) such as PNRs or chemical inhomogenity due to cations disordering in the long range order matrix. HRTEM images provide a clear picture that a large number of SROs, twin boundaries, discontinuous crystal planes,

inhomogeneous distribution of A-site cations, etc. are present in the NBAT-BT matrix which in turn favors the dielectric dispersion and anti-polar properties.

E. **Polarization behavior under applied electric field**:

It has been described in the previous studies that different kind of dielectric material and their energy density capacity can be calculated from P-E loop [4-8]. Among all dielectrics, relaxor-antiferroelectrics have shown the largest integrated area within their P-E loops to store the energy efficiently. The relaxor-antiferroelectrics are the only system which possesses both nonlinear and linear P-E regions (except for temperatures slightly above T_c in the first-order ferroelectrics); the linear antiferroelectric low-field region, the non-linear antiferroelectric region, and linear dielectric saturated region at extremely high field. The combination of nonlinear and linear P-E loops in first quadrant of P(E) hysteresis is suitable for high energy storage devices with fast discharge capacity. Fig. 6 (a) shows the slim relaxor-antiferroelectric hysteresis (as-grown samples) of the NBAT-BT system for the frequency 1 Hz over a wide range of temperatures. P-E loops for 1 and 10 Hz are given in the inset (Fig. 6 (a) for comparative study. These P-E loops become slimmer and centered with increase in temperature. Polycrystalline ceramic samples are very prone to electrical breakdown under high electric field applications. We used very moderate field ~ 50-60 kV/cm to investigate the P-E loops to avoid large leakage current. Leakage current was separately measured for the same electric fields and was found to be a few μA. The magnitudes of these currents were at least three orders less than the range of real break down current (ca. mA) for an insulating ceramics. It can also be seen from figure 5 (b) that leakage current decreases with increase in temperature which is a signature of

the positive temperature coefficient of resistance (PTCR), extremely useful for power/energy based devices as current-limiter [40].

F. Energy Density Capacity:

The linear-nonlinear part of P-E loop provides energy density ~ 0.4-0.6 J/cm^3 at 50 kV/cm until 100 °C that increases with increase in temperature and persists above T_m of relaxor-AFE phase transition. The shaded area in the inset of P-E loop (Fig. 6(b)) represents the energy stored by the system. The P-E loops become slimmer with increase in temperature, suggesting high potential to store the energy density. Inset of figure 6 (b) shows two types (area I and II) of shaded areas (yellow and grey) that represent the charge and discharge capacities. Using P-E data, the discharge (release) (U_d), and charge (U_c) (storage) energy densities were calculated using the following relation: U_d = area II, U_c = area I + area II. The charge-discharge efficiency (η) of the capacitors was calculated using the relation: $\eta = U_d/U_c$ x 100%. The efficiency of the NBAT-BT was 48 % at 300 K for applied electric field of 50 kV/cm. A similar range of efficiency was found for poly(vinylide fluoride-hexafluoropropylene) (PVDF-HFP) [41].

G. Conclusions:

In summary, relaxor-AFE lead-free NBAT-BT electroceramics were investigated for energy density applications. A small (~ 0.06%) substitution of Al^{3+} cations in NBAT-BT system near the MPB leads to development of short range order polar nano regions within an AFE matrix. XRD analysis elucidates the coexistence of mixed rhombohedral and tetragonal phases. HRTEM images suggest the presence of disordered crystals, chemical inhomogeneity, and conjunction of nano-size crystals with larger grains. Two step-like phase transitions were seen in

dielectric and tangent loss spectra, characteristic of relaxor-AFE to mixed AFE-FE phase at 80-120°C, and diffuse phase transition near 240°C. The lower phase transition shows large dielectric dispersion and follows a non-linear VF relation with freezing of PNRs at 34 °C. A pinched P-E hysteresis was observed over a wide range of temperatures that clearly suggests the coexistence of the relaxor-AFE phase even far above the T_m. Moderate energy density and low leakage current of 0.4-0.6 J/cm^3 and 1μA were obtained at 50 kV/cm, respectively. These features suggest that lead-free relaxor-AFE ceramics or thin films have commercial potential for energy storage applications.

Acknowledgement: Authors would like to acknowledge to Prof. J. F. Scott (Univ. of Cambridge, UK) for his critical evaluations and suggestions to improve the manuscript and Mr. K. N. Sood for his support in carrying out SEM.

Figure Captions:

Fig.1 (a) shows the Rietveld fitting of NBAT-BT XRD patterns with tetragonal crystal structure (space group P4mm) and (b) rhombohedra crystal structure (space group R3c); SEM image is given in the inset of figure 1(a).

Fig. 2 (a-f) HRTEM images of NBAT-BT crystals and lattice planes, , (a) HRTEM images of NBAT-BT nano- and micro-crystals, (b) ordered PNRs in the AFE matrix, (c-f) d-spacing of crystal planes (001), (110), (220), (111) respectively.

Fig. 3 (a) FFT image of the (101) and (110) planes of the r-phase and t-phase, (b) IFFT image of same FFT that shows the presence of twin phase boundaries and various SROs.

Fig. 4(a-d) Raman Spectra of NBAT-BT system with DHO model fitting (b) low (c) medium (d) high frequency regions.

Fig. 5 dielectric spectra (a) and tangent loss (b) as functions of temperature in the frequency range of (1 kHz-1 MHz), (c) non-linear VF relation fitting, (d) fitting of modified Curie-Weiss law near diffuse phase transition at 10 kHz.

Fig.6 (a) P-E loops hysteresis at different temperatures and moderate applied electric field (50 kV/cm), in inset, P-E loops at 1 and 10 kHz for comparison. (b) Leakage current as function applied electric field; right inset shows current density as function of temperatures. Shaded area (I) of P-E loop illustrates the capacity to store the energy (left inset)

Table:1 Simulation data of the Rietveld Analysis for two space group (R3c and P4mm) and crystal systems.

Phases	Atoms	X	Y	Z
Tetragonal *P4mm*	Bi	0.00	0.00	4.27949
	Ba	0.00	0.00	4.65655
	Na	0.00	0.00	4.95192
	Al	0.00	0.00	4.95192
	Ti	0.50	0.50	-5.35526
	O1	0.50	0.50	6.46282
	O2	0.50	0.00	5.58466

Reliability factors are R_p = *7.61 %*, R_{wp} = *10.4 %*, χ^2 = *2.09*, R_{exp} = 6.97 *% and* R_{Bragg} = *3.94%*

Phases	Atoms	X	Y	Z
Rhombohedral *R3c*	Bi	0.00	0.00	0.63378
	Ba	0.00	0.00	0.63378
	Na	0.00	0.00	0.63378
	Al	0.00	0.00	0.63378
	Ti	0.00	0.00	0.39033
	O	-0.05406	1.46715	1.11697

Reliability factors are R_p = 9.43*%*, R_{wp} = 12.1 *%*, χ^2 = *2.89*, R_{exp} = 6.98 *% and* R_{Bragg} = *5.46%*

Table 2. Stoichiometric details of the A-site elements for NBAT-BT crystal system.

Elements at A-site	Percentage of initial elemental compositions	Observed elemental compositions from SEM & HRTEM (±10% uncertainty)
Na	0.43	0.42
Bi	0.43	0.44
Ba	0.08	0.08
Al	0.06	0.06

References:

[1] S. A. Sherrill, P. Banerjee, G. W. Rubloff, and S.B. Lee, *Phys. Chem. Chem. Phys*., 2011, **13**, 20714.

[2] C. A. Paz de Araujo, J. D. Cuchiaro, L. D. Mcmillan, M. C. Scott, and J. F. Scott, Nature (London), 1995, **374**, 627.

[3] Baojin Chu, Xin Zhou, Kailiang Ren, Bret Neese, Minren Lin, Qing Wang, F. Bauer, Q. M. Zhang, Science, 2006, **313**, 334.

[4] H. Ogihara, C. A. Randall, and Susan Trolier-McKinstry, J. Am. Ceram. Soc., 2009, **92** [8] 1719.

[5] G. R. Love, ‘‘Energy Storage in Ceramic Dielectrics,’’ J. Am. Ceram. Soc., 1990, **73** [2] 323.

[6] Zhi-Min Dang, Jin-Kai Yuan , Sheng-Hong, and heng-Hong, Adv. Mater, 2013, **25**, 6334.

[7] N. Ortega, A. Kumar, J. F. Scott, D. B. Chrisey, M. Tomazawa, S. Kumari, D. G. B. Diestra, and R. S. Katiyar, J. Phys.: Condens. Matter., 2012, **24**, 445901.

[8] Tatiana M. Correia, Mark McMillen, Maciej K. Rokosz, Paul M. Weaver, John M. Gregg, Giuseppe Viola, and Markys G Cain, J. Am. Ceram. Soc., 2013, **96** [9] 2699.

[9] J. Y. Li , L. Zhang , and S. Ducharme , Appl. Phys. Lett., 2007, **90** , 132901.

[10] T. Takenaka, K. Maruyama, and K. Sakata, Jpn. J. Appl. Phys., 1991, **30**, 2236.

[11] R¨odel, W. Jo, K. T. P. Seifert, E.-M. Anton, and T. Granzow, J. Amer. Ceram. Soc., 2009, **9**2, 1153.

[12] B. J. Chu, D. R. Chen, G. R. Li, and Q R. Yin, J. Eur. Ceram. Soc., 2002, **22**, 2115.

[13] Yiping Guo, Mingyuan Gu, Haosu Luo, Yun Liu, and Ray L. Withers, Phys. Rev. B, 2011, **83**, 054118.

[14] D. Maurya, V. Petkov, A. Kumar, S. Priya, Dalton Transactions, 2012, **41 (18)**, 5643.

[15] V. Dorcet, G. Trolliard, and P. Boullay, Chem. Mater., 2008, **20**, 5061.

[16] V. Dorcet, G. Trolliard, and P. Boullay, J. Magn. Magn. Mater., 2009, **321**, 1758.

[17] C. Ma and X. Tan, Solid State Commun., 2010, **150**, 1497.

[18] C Ma, Hanzheng Guo, and Xiaoli Tan, Adv. Funct. Mater., 2013, **23**, 5261.

[19] T. Takenaka, K. Maruyama, and K. Sakata, Jpn. J. Appl. Phys., 1991, **30**, 2236.

[20] I. W. Kim, D. S. Lee, S. H. Kang, and C.W. Ahn, Thin Solid Films, 2003, **441**, 115.

[21] C. Xu, D. Lin, and K. W. Kwok, Solid State Sci., 2008, **10**, 934.

[22] Q. Xu, D.-P. Huang, M. Chen,W. Chen, H.-X. Liu, and B.-H. Kim, J. Alloys Compd., 2009, **471**, 310.

[23] Y. S. Sung, J. M. Kim, J. H. Cho, T. K. Song, M. H. Kim, H. H. Chong, T. G. Park, D. Do, and S. S. Kim, Appl. Phys. Lett., **2010**, 96, 022901.

[24] S. Zhang, A. B. Kounga, W. Jo, C. Jamin, K. Seifert, T. Granzow, J. R¨odel, and D. Damjanovic, Adv. Mater., 2009, **21**, 4716.

[25] C. Ma and X. Tan, J. Am. Ceram. Soc., 2011, **94 [11]**, 4040.

[26] Yiping Guo, Mingyuan Gu, Haosu Luo, Yun Liu, and Ray L. Withers, Phy. Rev. B, 2011, **83**, 054118.

[27] K. Yao, S. Chen, M. Rahimabady, S. Yu, Francis Eng Hock Tay, L. Lu, M. S. Mirshekarloo, and T. Sritharan: IEEE Transactions on Ultrasonics, Ferroelectrics, and Frequency Control, 2011, **58**, 1968.

[28] P. Kim, N. M. Doss, J. P. Tillotson, P. J. Hotchkiss, M.-J. Pan, S. R. Marder, J. Li, J. P. Calame, J. W. Perry, *ACS Nano*., 2009, **3**, 2581.

[29] V. Tomer, G. Polizos, E. Manias, and C. A. Randall, J. *Appl. Phys*., 2010, **108**, 074116.

[30] S. Puli Venkata, A. Kumar, D. B. Chrisey, M. Tomazawa, J. F. Scott, and R. S. Katiyar, *J. Phys. D: Appl. Phys*. 2011, **44**, 395403.

[31] Wook Jo, John E. Daniels, Jacob L. Jones, Xiaoli Tan, Pamela A. Thomas, Dragan Damjanovic, and Jürgen Rödel, Journal of Applied Physics, 2011, **109**, 014110.

[32] D. T. Cromer, J. Phys. Chem. 1957, **61**, 753.

[33] R. S. Katiyar, J. F. Ryan, and J. F. Scott, Phys. Rev. B 1971, **4**, 2635.

[34] J. Suchanicz, I J-Sumara, T. K. Kruzina, J Electroceram, 2011, **27**, 45.

[35] M. Zhang, J. F. Scott, I.A. Zvirgds, Ferroelectrics, 1986, **6**, 147.

[36] I. G. Siny, E. Husson, I. M. Beny, S. G. Lushnikov, E. A. Rogacheva, P. P. Syrnikov, Physica B, 2001, **293**, 382.

[37] H. Vogel, *Z. Phys*. 1921, **22**, 645.

[38] A. K. Tagantsev, *Phys. Rev. Lett*. 1994, **72**, 1100.

[39] I. Rivera, A. Kumar, N. Ortega, R. S. Katiyar, and S. Lushnikov, *Solid State Commun*. 2009, **149**, 172.

[40] A. Kumar, R. S. Katiyar, and J. F. Scott, Applied physics letters, 2009, **94**, 212903.

[41] S. Zhang, Q. Zhang. High Energy density polymeric compositions, methods of the manufacture, and articles comprising the same. *Patent No. US 2010/0067172 A1*.

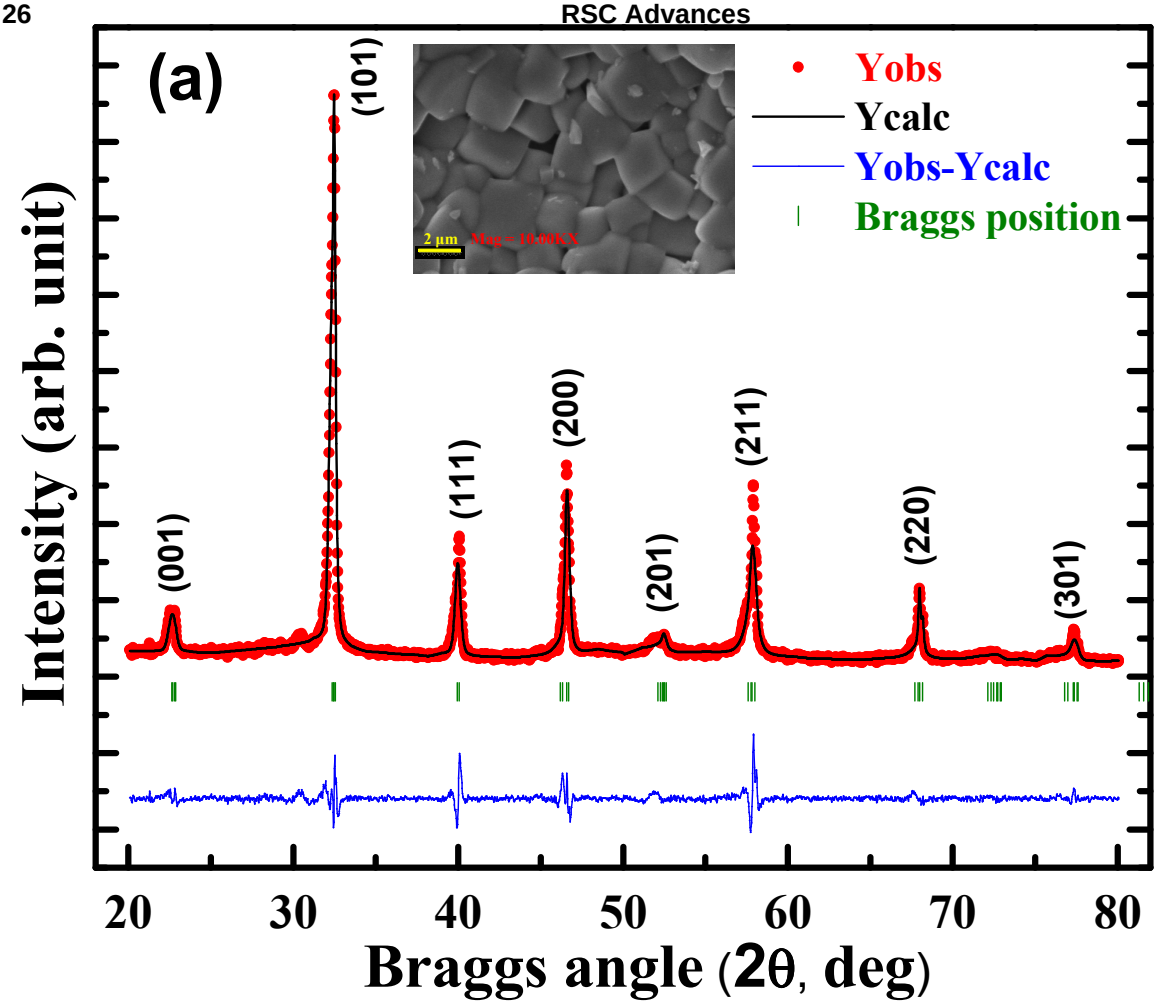

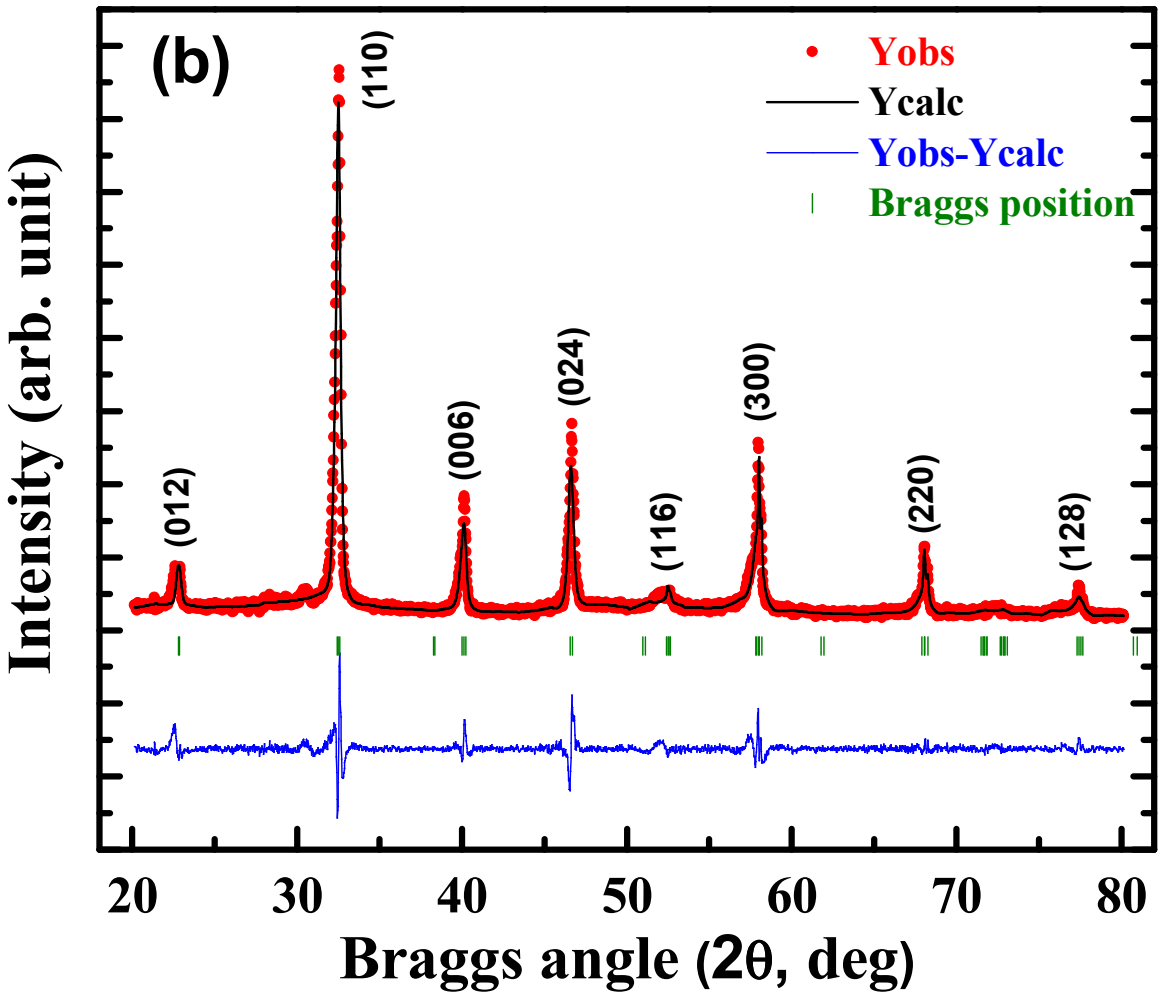

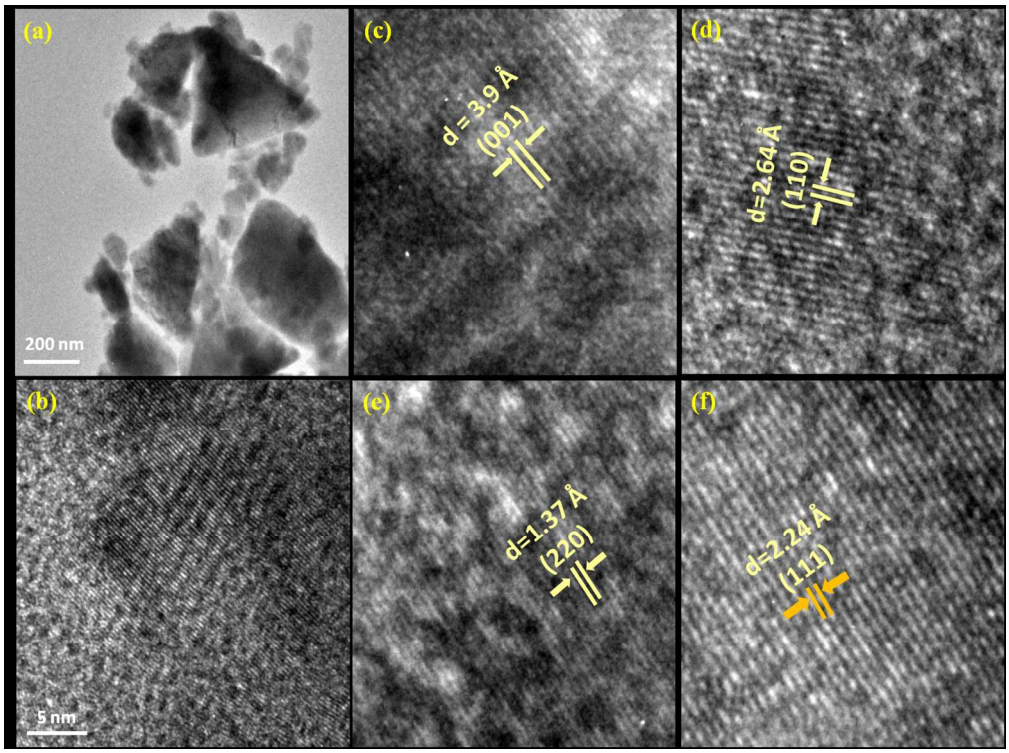

256x190mm (150 x 150 DPI)

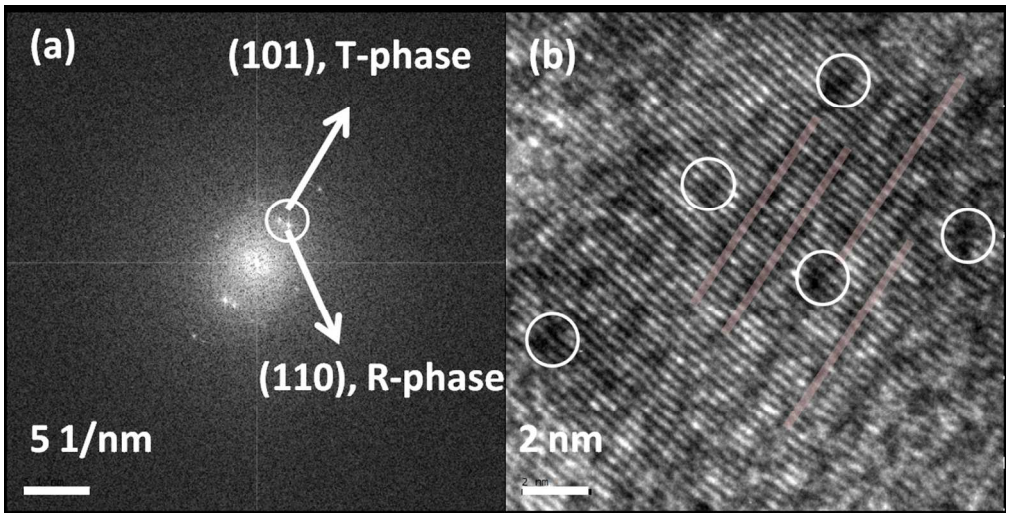

204x103mm (150 x 150 DPI)